

SF-Loc: A Visual Mapping and Geo-Localization System based on Sparse Visual Structure Frames

Yuxuan Zhou, Xingxing Li*, Shengyu Li, Chunxi Xia, Xuanbin Wang, Shaoquan Feng

Abstract—For high-level geo-spatial applications and intelligent robotics, accurate global pose information is of crucial importance. Map-aided localization is a universal approach to overcome the limitations of global navigation satellite system (GNSS) in challenging environments. However, current solutions face challenges in terms of mapping flexibility, storage burden and re-localization performance. In this work, we present SF-Loc, a lightweight visual mapping and map-aided localization system, whose core idea is the map representation based on sparse frames with dense but compact depth, termed as visual structure frames. In the mapping phase, multi-sensor dense bundle adjustment (MS-DBA) is applied to construct geo-referenced visual structure frames. The local co-visibility is checked to keep the map sparsity and achieve incremental mapping. In the localization phase, coarse-to-fine vision-based localization is performed, in which multi-frame information and the map distribution are fully integrated. To be specific, the concept of spatially smoothed similarity (SSS) is proposed to overcome the place ambiguity, and pairwise frame matching is applied for efficient and robust pose estimation. Experimental results on the cross-season dataset verify the effectiveness of the system. In complex urban road scenarios, the map size is down to 3 MB per kilometer and stable decimeter-level re-localization can be achieved.

Index Terms—Dense bundle adjustment, multi-sensor fusion, visual localization and mapping, place recognition

I. INTRODUCTION

Global localization is a critical problem in robotics and autonomous driving applications [1], [2]. For outdoor scenarios, global navigation satellite system (GNSS) is a commonly used technology for achieving global drift-free localization [3]. However, precise GNSS generally relies on high-precision services and products, while low-cost GNSS can hardly provide stable and accurate localization solutions in complex environments [4]. Map matching is another method for achieving global localization. By associating observations of the surrounding environment from external sensors widely equipped on intelligent devices (such as cameras) with a priori maps, different levels of global localization can be achieved, depending on the map representation [5], [6].

To achieve the practicality of map-aided localization, both the mapping and the re-localization phases should be carefully addressed. As to the mapping phase, the efficiency of map

This work was supported by the the National Science Fund for Distinguished Young Scholars of China (42425401), the National Natural Science Foundation of China (423B240), the National Key Research and Development Program of China (2023YFB3907100), and the "Sharp Knife" Technology Research Project of Science and Technology Department of Hubei Province (2023BAA025). (Corresponding author: Xingxing Li.)

The authors are with School of Geodesy and Geomatics, Wuhan University, China (e-mail: xingxingli@whu.edu.cn).

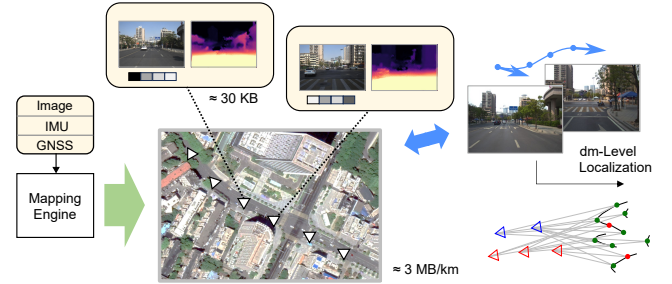


Fig. 1. Illustration of the SF-Loc system. The system is built upon the map representation of visual structure frames, which contain compressed image, compact depth information and global descriptor. The map sparsity is intentionally maintained, which ensures lightweight storage (≈ 3 MB/km) while keeps the ability of high-recall, decimeter level re-localization.

construction, the accuracy of the map elements and the storage burden of map data are some of the key factors. Considering the need of incremental mapping and crowd-sourced map updating, the flexibility of the map representation is also crucial. Current map forms, like vector map [7], 3D point cloud [8], [9], occupancy grid [10] and neural representations [11], [12], still cannot meet the above requirements perfectly, especially when considering vision-based schemes.

As to re-localization, the system functionality is highly coupled with the map representation. High recall and high localization accuracy generally need more detailed and distinguishable information of the environment, which seems contradictory with the expectation of a lightweight map. How to choose a practical map representation that meets the need of efficient mapping and effective re-localization, and develop a pipeline properly adapted to the representation, is the main concern of this work.

In this work, we propose SF-Loc, a lightweight visual mapping and map-aided localization system based on sparse visual structure frames. The visual structure frame is defined as a geo-tagged image frame with compressed RGB map and full-view depth map, which itself supports standalone and flexible re-localization. The word “structure” comes from two aspects, as the frame stores the environmental structure information (in the depth form), and the map frames are sparsely structured with special consideration for efficient association and reducing redundancy. Based on the concept, SF-Loc provides a pipeline for the auto-generation of visual structure frames through multi-sensor dense bundle adjustment (MS-DBA), as well as an implementation for coarse-to-fine map-based localization. The contributions of this work are listed as follows:

1) We provide a pipeline for large-scale mapping based on the visual-structure-frame map representation, which is built upon the integration of deep dense bundle adjustment and multi-sensor factor graph optimization (FGO).

2) We provide a coarse-to-fine map-aided localization pipeline which fully utilizes deep place recognition, local feature matching and spatial-temporal information association.

3) Real-world, cross-season experiments are conducted to validate different phases of the system.

4) The code is made open-source¹ to benefit the community.

II. RELATED WORK

A. VSLAM with multi-sensor fusion

Visual SLAM, which has been extensively studied in the past decade, is considered an effective and low-cost solution for relative pose estimation and mapping. Considering the form of visual information, point features [8], [13], line features [14] and direct photometric errors [15] have been exploited. By integrating IMU [16]–[18], GNSS [3], [19], and other sensors [20], the practicality of VSLAM can be improved in terms of robustness, continuity, accuracy and geo-referencing functionality. On this basis, multi-session and multi-agent SLAM systems are developed [21], [22]. Learning-based VSLAM frameworks are also investigated in recent implementations, covering neural representations [23], [24], data-driven association [25]–[27] and end-to-end pipelines [28], [29].

For map reuse of multi-sensor integrated VSLAM, obtaining globally smoothed pose estimation in the geographic coordinate system is important, as it impacts the absolute accuracy of the map and the practicality of user-side localization.

B. Visual place recognition

Visual place recognition (VPR) is a long-existing problem, which plays a crucial role in loop closure, multi-session mapping, re-localization and so on. Early approaches use handcrafted models (like bag-of-words [30] and VLAD [31]) to aggregate local feature descriptors, thus to evaluate the scene similarity. To overcome the long-term change challenge, sequential information is utilized [32].

In the last decade, deep neural network (DNN)-based methods, like NetVLAD [33], have greatly improved the practicality and accuracy of VPR. Following this trend, TransVPR [34] uses the transformer to incorporate multi-level attention mechanisms and improve the VPR performance. CosPlaces [35] transforms the place recognition problem from contrastive learning to a classification problem, which enables efficient training on 10-million-level large-scale datasets and is further enhanced with better viewpoint robustness [36]. AnyLoc [37] utilizes the visual foundation model to achieve ubiquitous VPR for different scenarios. It is noted that, most existing methods don't consider comprehensively the spatial distribution of database images and user-side relative poses, which could serve as powerful information to improve the stability of VPR.

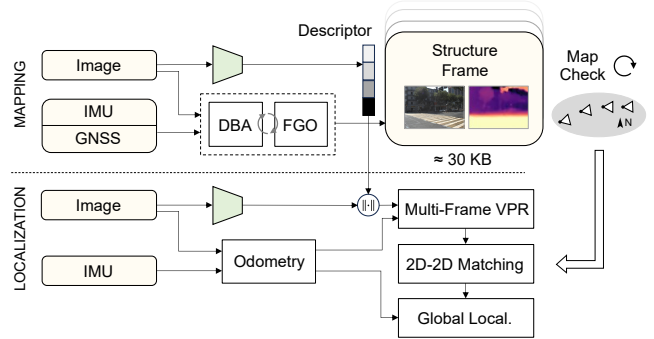


Fig. 2. The overall pipeline of the system, which is divided into the mapping phase and the localization phase.

C. Fine-grained visual re-localization

For high-accuracy visual re-localization (e.g. decimeter- or centimeter-level), it is generally needed to perform feature- or instance-level association between user perception and the map elements. Many of these methods follow a coarse-to-fine pipeline. In ORB-SLAM3 [8] and VINS-Mono [16], re-localization is performed through bag-of-words-based place recognition and pointwise matching between new feature observations and the point cloud map. Such pipeline is further improved in HLoc [9], where the power of deep learning is fully utilized in both mapping and localization phases. Besides, monocular depth prediction is exploited in [39] to achieve map-free visual re-localization.

Along with these methods, other approaches try to exploit higher-level information for map matching. Instance-level object modeling is integrated into classic VSLAM systems to overcome viewpoint variation and achieve long-term consistency [40]–[43]. In recent works, bird's-eye view (BEV) features are utilized to associate with priori vector maps to achieve accurate pose estimation, both for outdoor [44] and indoor scenarios [45]. The tradeoff of semantic-based re-localization is the loss of low-level, sometimes subtle but distinguishable, visual cues, which might lead to higher ambiguity.

III. SYSTEM OVERVIEW

The proposed system is built upon the concept of the visual-structure-frame-based map representation, and is mainly divided into the mapping phase and the localization phase, as shown in Fig. 2.

In the mapping phase, multi-sensor information is used to generate the feature-free map frames with recovered dense depth. Global co-visibility graph optimization is performed periodically in a low frequency to achieve global optimal pose estimation. On this basis, the local co-visibility is checked to keep the map sparsity and to achieve incremental mapping. Besides, a DNN-based VPR model is employed to compute the global descriptors of map frames.

In the localization phase, deep visual place recognition and feature matching models are exploited to achieve coarse-to-fine localization. During this process, multi-frame information and the map frame distribution are fully considered to improve the recall rate and the accuracy.

¹<https://github.com/GREAT-WHU/SF-Loc>

One principle behind the proposed map representation is to keep the visual information raw and non-encoded. The first advantage of doing so is that it ensures users have flexibility when using the map, without being constrained by any intermediate forms of information. The second advantage is that, the compression of a raw image is effective by applying mature techniques like JPEG [46], without losing the dominant geometric or appearance information.

IV. MAPPING PHASE

In this phase, the implementation details of the mapping phase are presented.

A. Multi-Sensor Dense Bundle Adjustment

The concept of dense bundle adjustment (DBA) is proposed in [26], which is inherited in this work. Specifically, sequential images are fed into a convolutional neural network (CNN) with gated recurrent units (GRUs) to compute dense optical flows among co-visible image pairs. To explain this, consider the rigid flow produced by dense projection of one image pair (source frame i projected to target frame j)

$$\mathbf{u}_{ij} = \Pi_c(\mathbf{T}_{ij} \circ \Pi_c^{-1}(\mathbf{u}_i, \lambda_i)), \quad \mathbf{T}_{ij} = \mathbf{T}_j \circ \mathbf{T}_i^{-1} \quad (1)$$

where Π_c is the camera projection model, \mathbf{T}_{ij} is the relative camera pose, \mathbf{u}_i denotes the $n = (H/8) \times (W/8)$ grid-like 2D points in the image frame, λ_i is the inverse depth map.

The optical flow module takes the CNN-encoded image feature map and the rigid flow as input and outputs the corrected optical flow (in the residual form) together with the weight \mathbf{w}_{ij} , which leads to the following error equation

$$\underbrace{(\delta \mathbf{u}_{ij})_{2n \times 1}}_{\mathbf{r}} = \underbrace{[\mathbf{J}_i \quad \mathbf{J}_j \quad \mathbf{J}_{\lambda_i}]}_{\mathbf{J}} \underbrace{\left[\begin{array}{c} \xi_i^\top \quad \xi_j^\top \quad (\delta \lambda_i)^\top \end{array} \right]_{n \times 1}}_{\mathbf{x}} \quad (2)$$

where ξ_i, ξ_j are Lie algebras of the camera poses, $\mathbf{J}_i, \mathbf{J}_j, \mathbf{J}_{\lambda_i}$ are Jacobians derived from (1).

The residual-form dense optical flows are treated as re-projection errors, which are further used for bundle adjustment to simultaneously estimate the poses and dense depths of the images. Furthermore, the estimated poses and depths are recurrently fed back into the optical flow module, thus to iteratively refine all the geometric information. This process is end-to-end trainable, which shows good generalization in real-world scenes with synthetic training [26].

In our early work [48], we demonstrate the possibility of tightly integrating DBA with multi-sensor information. To be specific, the Hessian form of (2) is derived and stacked for all projections from frame i , leading to

$$\begin{bmatrix} \mathbf{v}_i \\ \mathbf{z}_i \end{bmatrix} = \begin{bmatrix} \mathbf{B}_i & \mathbf{E}_i \\ \mathbf{E}_i^\top & \mathbf{C}_i \end{bmatrix} \begin{bmatrix} \xi_{i,1,2,\dots,N} \\ \delta \lambda_i \end{bmatrix} \quad (3)$$

where $\xi_{i,1,\dots,N}$ is the stacked Lie algebras of camera poses.

The dense depth states are further eliminated through Schur complement to construct a compact constraint among the poses, following

$$\underbrace{(\mathbf{B}_i - \mathbf{E}_i \mathbf{C}_i^{-1} \mathbf{E}_i^\top)}_{\mathbf{H}_{c,i}} \xi_{i,1,\dots,N} = \underbrace{\mathbf{v}_i - \mathbf{E}_i \mathbf{C}_i^{-1} \mathbf{z}_i}_{\mathbf{v}_{c,i}} \quad (4)$$

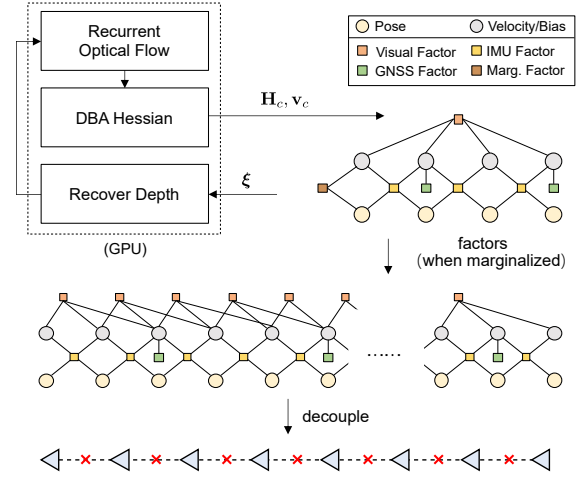


Fig. 3. Illustration of the proposed multi-sensor DBA. 1) A sliding window factor graph is used for real-time state estimation and depth estimation, which is tightly integrated with the recurrent optical flow module. 2) The global factor graph collects the marginalized factors and provides low-frequency, long-time smoothed optimization results. 3) After mature, the frames in the global factor graph are decoupled to serve as standalone visual structure frames and inserted into the map.

in which the inversion operation of \mathbf{C}_i is efficient as it is a diagonal matrix.

The Hessian-form pose constraint, which embeds the DBA information of co-visible images, is fed to a sliding-window factor graph based on GTSAM [47] for multi-sensor fusion, as shown in Fig. 3. A generic graph design is employed, which allows for flexible integration of different kinds of sensors or information. The states in the graph are as follows

$$\mathbf{x}_k = (\mathbf{T}_{b_k}^w \quad \mathbf{v}_{b_k}^w \quad \mathbf{b}_k), \quad k \in \mathcal{K} \quad (5)$$

$$\mathbf{T}_{b_k}^w = \begin{bmatrix} \mathbf{R}_{b_k}^w & \mathbf{t}_{b_k}^w \\ 0 & 1 \end{bmatrix} \in SE(3), \quad \mathbf{b}_k = (\mathbf{b}_{a,k} \quad \mathbf{b}_{g,k}) \quad (6)$$

where \mathcal{K} is the frame set of the sliding window, $\mathbf{T}_{b_k}^w$ is the body (IMU) poses in the world frame, $\mathbf{v}_{b_k}^w$ is the velocity, $\mathbf{b}_{a,k}$ and $\mathbf{b}_{g,k}$ are accelerometer/gyroscope biases.

Without losing generality, the following factors are considered in this work:

1) Visual factor:

$$\mathbf{E}_c(\mathbf{x}_c) = \frac{1}{2} \mathbf{x}_c^\top \mathbf{H}_c \mathbf{x}_c - \mathbf{x}_c^\top \mathbf{v}_c \quad (7)$$

where $\mathbf{H}_c, \mathbf{v}_c$ are the Hessian matrix and vector of DBA (stacked from $\mathbf{H}_{c,i}, \mathbf{v}_{c,i}$) with all the depth states eliminated, \mathbf{x}_c is the related camera poses. To associate the camera poses with the IMU-centered pose states, the IMU-camera extrinsics are used to transform (7), as detailed in [48].

2) IMU factor:

$$\mathbf{r}_b(\mathbf{x}_k, \mathbf{x}_{k+1}) = \begin{bmatrix} \mathbf{R}_{b_k}^w \top \left(\mathbf{p}_{b_{k+1}}^w - \mathbf{p}_{b_k}^w + \frac{1}{2} \mathbf{g}^w \Delta t_k^2 - \mathbf{v}_{b_k}^w \Delta t_k \right) - \Delta \tilde{\mathbf{p}}_{b_{k+1}}^{b_k} \\ \mathbf{R}_{b_k}^w \top \left(\mathbf{v}_{b_{k+1}}^w + \mathbf{g}^w \Delta t_k - \mathbf{v}_{b_k}^w \right) - \Delta \tilde{\mathbf{v}}_{b_{k+1}}^{b_k} \\ \text{Log} \left(\left(\mathbf{R}_{b_k}^w \right)^{-1} \mathbf{R}_{b_{k+1}}^w \left(\Delta \tilde{\mathbf{R}}_{b_{k+1}}^{b_k} \right)^{-1} \right) \\ \mathbf{b}_{a,k+1} - \mathbf{b}_{a,k} \\ \mathbf{b}_{g,k+1} - \mathbf{b}_{g,k} \end{bmatrix} \quad (8)$$

where $\Delta\tilde{\mathbf{p}}_{b_{k+1}}^{b_k}$, $\Delta\tilde{\mathbf{v}}_{b_{k+1}}^{b_k}$, $\Delta\tilde{\mathbf{R}}_{b_{k+1}}^{b_k}$ are the IMU preintegration terms [49], \mathbf{g}^w is the gravity vector, Δt_k is the time interval.

3) GNSS factor:

$$\mathbf{r}_g(\mathbf{x}_k) = \mathbf{T}_w^n \circ \mathbf{T}_{b_k}^w \circ \mathbf{t}_g^b - \tilde{\mathbf{p}}_g^n \quad (9)$$

where $\tilde{\mathbf{p}}_g^n$ is the measured position of the GNSS phase center in the navigation frame, \mathbf{t}_g^b is the IMU-GNSS lever-arm, \mathbf{T}_w^n is a fixed world-to-navigation transformation obtained through the initial alignment.

Probabilistic marginalization is applicable to the above factor graph, following the common operation based on Schur complement [17]. For DBA information, a sub-graph related to the oldest frame is temporarily constructed to generate the marginalization information. Considering the marginalization term, the overall cost function of the sliding-window factor graph is defined as follows

$$\begin{aligned} \min \quad & \mathbf{E}_m(\mathbf{x}) + \mathbf{E}_c(\mathbf{x}_c) \\ & + \sum_{k \in \mathcal{K}} \|\mathbf{r}_b(\mathbf{x}_k, \mathbf{x}_{k+1})\|_{\Omega_b}^2 + \sum_{k \in \mathcal{G}} \rho_C \left(\|\mathbf{r}_g(\mathbf{x}_k)\|_{\Omega_g}^2 \right) \end{aligned} \quad (10)$$

where $\mathbf{E}_m(\mathbf{x})$ is the marginalization term in the quadric cost function form, Ω_b and Ω_g are uncertainties of the factors, $\rho_C(\cdot)$ is the Cauchy loss function.

After the factor graph optimization, the corrected poses are substituted back to Eq. (3) to recover the dense depths

$$\delta \lambda_i = \mathbf{C}_i^{-1}(\mathbf{z}_i - \mathbf{E}_i^\top \boldsymbol{\xi}_{i,1,\dots,N}) \quad (11)$$

then the estimated poses and depths are fed back into the optical flow module to refine the optical flows and adjust the weights. For every projection, the optical flow module will be recurrently called for several times until mature. The overall process simultaneously adjust the pose estimation, the dense data association and the depths, trying to achieve consistency of the above information.

An issue that should be considered is the obtainment of global optimal pose estimation. This is important both for monocular visual-inertial odometry (due to the dynamic-dependent observability) and GNSS-integrated navigation (due to intermittent GNSS availability), which can't be simply achieved in a sliding-window estimator. In our system, we maintain a global factor graph, which collects the marginalized factors from the sliding-window factor graph. The objective of the global factor graph is written as follows

$$\begin{aligned} \min \quad & \sum_{k \in \mathcal{K}_{\text{all}}} \mathbf{E}_{c,k}(\mathbf{x}_{c,k}) + \sum_{k \in \mathcal{K}_{\text{all}}} \|\mathbf{r}_b(\mathbf{x}_k, \mathbf{x}_{k+1})\|_{\Omega_b}^2 \\ & + \sum_{k \in \mathcal{G}_{\text{all}}} \rho_C \left(\|\mathbf{r}_g(\mathbf{x}_k)\|_{\Omega_g}^2 \right) \end{aligned} \quad (12)$$

where $\mathbf{E}_{c,k}(\mathbf{x}_{c,k})$ is the DBA information that takes frame k as the source frame, $\mathbf{x}_{c,k}$ is the related camera poses. Each $\mathbf{E}_{c,k}$ reflects the local co-visibility around frame k .

This global factor graph includes all the information related to the poses, velocities and IMU biases, while it can still be solved efficiently thanks to the locality of the problem. Compared to pose-only pose graph estimation (PGO) [38], this graph contains complete IMU information and Hessian-form visual information, which can better smooth low-observability periods with future information.

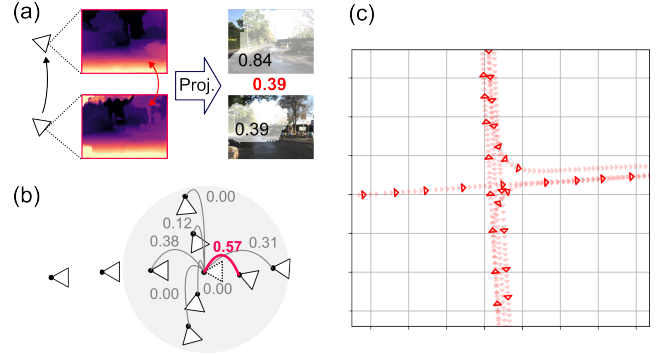


Fig. 4. Illustration of the co-visibility checking. (a) Co-visibility for one image pair; (b) Local co-visibility checking, the dashed-line frame won't be inserted due to significant co-visibility with one nearby frame; (c) An example of the sparsified structure frame map.

B. Map Construction and Maintenance

After the global pose optimization, we extract the frame pose from the global graph, pack the RGB image (with JPEG compression), the low-resolution depth map and the global descriptor produced by some VPR model together to construct a visual structure frame, then insert it into the map. To make the map lightweight, it is important to keep the sparsity of the visual structure frames without sacrificing too much of the effectiveness of user-side re-localization. Besides, considering the application scenario of multi-session mapping, the system should support incremental update.

Fortunately, this can be simply achieved based on the flexible model-free, frame-based map representation of SF-Loc. To be specific, the local co-visibility is checked to select new frames to be added into the map. The co-visibility is efficiently computed based on the bi-directional dense rigid flow that falls within the field of view, following

$$\tau(\mathbf{T}_i, \mathbf{T}_j, \boldsymbol{\lambda}_i) = \frac{\text{count}(\mathbf{u}_{ij}.\text{inside}(0, 0, H, W))}{H \cdot W} \quad (13)$$

$$\text{covis}(\mathbf{T}_i, \mathbf{T}_j, \boldsymbol{\lambda}_i, \boldsymbol{\lambda}_j) = \min(\tau(\mathbf{T}_i, \mathbf{T}_j, \boldsymbol{\lambda}_i), \tau(\mathbf{T}_j, \mathbf{T}_i, \boldsymbol{\lambda}_j)) \quad (14)$$

where \mathbf{u}_{ij} is the rigid flow in Eq. (1), H , W are the height and width of the image. The illustration of the co-visibility is presented in Fig. 4.

The co-visibility directly reflects the overlapping of different frames. With the intention of avoiding redundant map frames, we simply select frames with relatively low co-visibility when adding frames to the map. The co-visibility threshold Ξ controls the mapping process, which reflects the trade-off between data size and re-localization performance. We select $\Xi = 0.4$ as the typical value, which indicates that for one query along the smooth trajectory between two nearby map frames, an optimistic $(1.0 + 0.4)/2 = 0.7$ overlapping can be expected.

When adding/removing/updating frames to the map, it is not necessary to perform data association across nearby frames or reconstruct the 3D model, as every visual structure frame works fully independently. This makes the mapping phase highly flexible, and can be easily applied to multi-session mapping or incremental map updating.

V. MAP-AIDED LOCALIZATION PHASE

In this phase, the implementation details of the map-aided localization are presented, which follows the coarse-to-fine process proposed in [9]. Based on state-of-the-art place recognition and feature matching techniques, specially designed methods which considers temporal integration are proposed to adapt to the map representation and to maximize the performance in real-world scenarios.

A. Multi-Frame Place Recognition

We use lightweight CNN-based methods (e.g., [33], [35], [36], [52]) to compute global descriptors and to evaluate the similarity between the query image and map frames. On this basis, we develop a model-driven technique to integrate sequential queries and map frame distribution to improve the robustness and stability of the coarse localization.

The necessity of multi-frame place recognition lies in the existence of repetitive and featureless scenes in the real world, which leads to inevitable spatial ambiguity. To handle this, it is natural to take into account the environmental cues within a larger range to resolve the ambiguity. Notice that we call this process “multi-frame place recognition” rather than “sequential place recognition”, as the map frames are generally not “sequential” but are “randomly” distributed in the geographic space.

To avoid the ambiguity of single-shot VPR, we propose an metric called spatially smoothed similarity (SSS) that combines the information of appearance similarity, map distribution and user-side relative poses. To be specific, we set particles around every landmark frames in the map, with every particle to be a 2D pose (x, y, θ) that represents a candidate of the query pose. With the help of the user-side odometry, we compute the virtual trajectory of every particle, following

$$(\mathbf{T}^i)_{4 \times 4 \times L} = \mathbf{T}_{p_i}^w \left\{ \mathbf{T}_{c_{k+1-j}}^{c_k} \right\}_{j=1,2,\dots,L}, i \in \mathcal{P} \quad (15)$$

where \mathcal{P} is the particle candidate set, L is the window size used for multi-frame VPR.

For every particle, we efficiently search for the spatially nearest map frame corresponding to every history pose through KD-Tree. This leads to a sequence of L2 distances for every particle

$$(\text{id}x^i)_{L \times 1} = \text{db.nearest}(\mathbf{T}^i), i \in \mathcal{P} \quad (16)$$

$$(\sigma^i)_{L \times 1} = \sigma [\text{id}x^i], i \in \mathcal{P} \quad (17)$$

where db is the map database organized by a spatial KD-Tree, σ is the $L \times M$ similarity matrix which stores the L2 similarities between the L query frames and all M frames in the map. The similarity computation is performed every time a new query frame comes and stored in the memory.

Then, we compute the SSS distance by averaging the L2 distances

$$\sigma_{\text{SSS}}^i = \|\sigma^i\|/\sqrt{L}, i \in \mathcal{P} \quad (18)$$

and the particle with minimum σ_{SSS}^i is taken as the retrieved map frame.

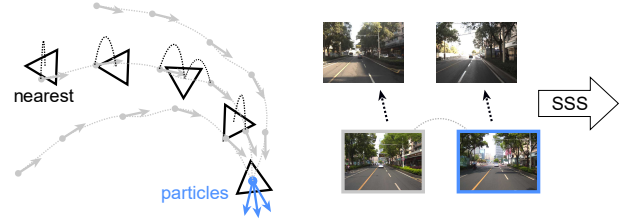


Fig. 5. Illustration of the multi-frame place recognition. Particles that indicate the query pose are set around map frames. The user-side trajectory is used for nearest searching to associate with the map frames, then the SSS distance is evaluated, which combines the information of multiple image pairs.

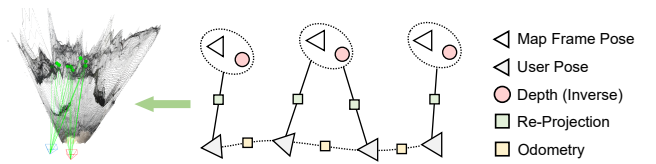


Fig. 6. Illustration of the multi-frame fine localization. Pairwise query-to-map correspondences are computed and stored to construct a factor graph, in which the depth uncertainty and matching errors can be carefully handled.

The rationality of SSS is based on the assumption that the historical images of a correctly recalled query should also exhibit high similarity to their spatially adjacent map frames. The geographical distribution of map frames (which is obtained in the mapping phase), along with user-side pose information, is implicitly incorporated to the metric in nearest neighbor search. This technique can be easily adopted to common VPR models without extra layers or finetuning, transforming single-frame VPR similarities to multi-frame ones.

In our implementation for outdoor environments, we simply set 3 particles around every map frame, corresponding to the 2D poses $(0, 0, 0^\circ)$, $(0, 0, -30^\circ)$, $(0, 0, 30^\circ)$ relative to the map frame pose.

B. Fine Pose Estimation

After successful retrieval of the map frame corresponding to the query image, fine-grained re-localization can be performed. In our system, this process could be achieved based on one single map frame and is independent of any re-constructed model, considering that the visual structure frame contains the full-view depth. This makes the re-localization simple and highly flexible.

Specifically, 2D-2D matching between the query frame and the map frame is performed based on feature extraction method like Superpoint [53] and matching techniques like Lightglue [50] or Superglue [51]. With the 2D-2D correspondences and the full-view depth contained in the map frame, several techniques can be applied to estimate the pose of the query image, like perspective-n-point (PnP) or just aligning the two-view reconstruction result with the metric-scale depth. To improve the robustness, RANSAC can be used.

Despite the simplicity, the above methods couldn't be directly used for multi-frame matching. In the application scenarios that our system concerns (cross-season, dynamic objects, etc.), robust feature matching is hard to promise, even

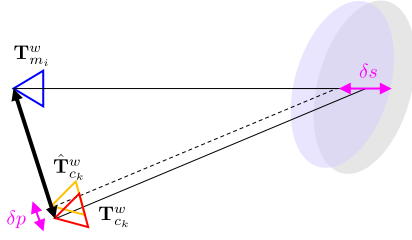


Fig. 7. Illustration of how depth uncertainty of the map frame affects the user pose estimation accuracy. In the figure, δs denotes the scale uncertainty of the depth map, δp denotes the position error of user-side localization. An approximate $\delta p \propto \delta s \cdot |t_{c_k}^{m_i}|$ relationship can be found.

with state-of-the-art learning-based techniques. To maximize the success rate and provide accurate pose estimation under large amounts of outliers, we combine multi-frame correspondences and the odometry in a factor graph, as shown in Fig. 6. For better efficiency, we don't do exhaustive matching among all the related frames. Instead, we compute the correspondences between every query-to-database image pair from VPR. Based on the re-projection errors, the cost function of the multi-frame pose estimation is written as follows

$$\min \sum_{k \in \mathcal{K}} \left\| \mathbf{T}_{c_{k+1}}^{w-1} \circ \mathbf{T}_{c_k}^w \circ \hat{\mathbf{T}}_{c_{k+1}}^{c_k} \right\|_{\Omega_p}^2 + \sum_{k \in \mathcal{K}} \sum_{f \in \mathcal{F}_{k,i}} \left\| \lambda_f^{m_i} - \hat{\lambda}_f^{m_i} \right\|_{\Omega_\lambda}^2 + \sum_{k \in \mathcal{K}} \sum_{f \in \mathcal{F}_{k,i}} \rho_C \left(\left\| \pi_c \left(\mathbf{T}_{m_i}^{c_k} \circ \pi_m^{-1} \left(\mathbf{u}_f^{m_i}, \lambda_f^{m_i} \right) \right) - \mathbf{u}_f^{c_k} \right\|_{\Omega_c}^2 \right) \quad (19)$$

where $\hat{\mathbf{T}}_{c_{k+1}}^{c_k}$ is the relative pose estimation, $\hat{\lambda}_f^{m_i}$ is the sampled inverse depth of point f on the map frame m_i , $\mathcal{F}_{k,i}$ is the matched feature point set between map frame m_i and user-side frame c_k , $\mathbf{u}_f^{m_i}$ and $\mathbf{u}_f^{c_k}$ are the point coordinates respectively, Ω_p , Ω_λ , Ω_c are the uncertainties. Notice that the map frame poses are fixed due to unobservability of the reference.

Another concern about the re-localization is that, does the depth estimated by monocular DBA enough for high-precision re-localization? A rough answer is that the fine-grained visual localization doesn't need decimeter-level depth to achieve decimeter-level pose estimation. An intuitive example is illustrated in Fig. 7. As is shown, the re-localization error is proportional to the product of the depth (or rather scale) error and the recall distance. Given 10% depth error of the map frame and < 10 m recall distance, we can still expect a < 1 m re-localization accuracy, which is enough for the applications that we care about. Actually, considering the demand of robust re-localization, correct image retrieval and feature matching are more important than the accuracy of structure information, which allow us to store the depth of the map frame in a highly compact way (i.e., $\times 8$ downsampled).

In the later experimental part, we will discuss the performance of different pose estimation methods.

VI. EXPERIMENTS

In the experimental part, different modules of the system, including multi-sensor mapping, place recognition and fine re-localization are comprehensively tested.

To fully evaluate the mapping and localization performance of the system in complex conditions, we use the self-made

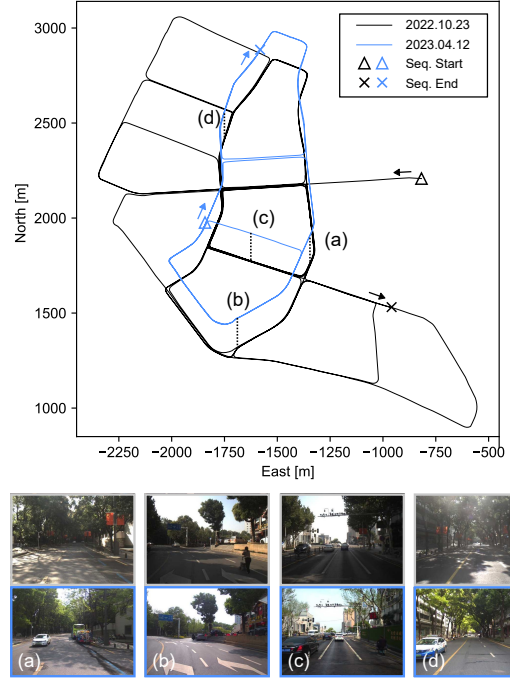


Fig. 8. Vehicle trajectories and example images of the experimental dataset. The data sequence collected in 2022/10/23 (5400 sec duration, 30 km mileage, 16 km one-way road coverage) is used for mapping, while the data sequence collected in 2023/04/12 (1800 sec duration, 10 km mileage, 4.9 km one-way road coverage) is used for localization.

multi-sensor dataset collected in Wuhan City on 2022/10/23 and 2023/04/12 respectively. The trajectories of the two sequences are shown in Fig. 8. To be specific, the data sequence on 2022/10/23 is used to evaluate the performance of incremental mapping, with multiple revisits of the same road segments. The data sequence on 2023/04/12 is used to evaluate the map-aided localization, which is challenging considering the cross-season condition and the high vegetation coverage rate of the environment.

The experimental vehicle is equipped with RGB cameras, an ADIS16470 IMU, a Septentrio AsteRx4 GNSS receiver and a tactical-grade IMU for reference use. The sensor installation and the camera lens are different for the two dates. A nearby base station is used for differential GNSS (DGNSS) processing. The smoothed trajectory of post-processing DGNSS/INS integration based on high-end IMU is taken as the ground truth, which is featured with centimeter-to-decimeter level position accuracy.

In the mapping phase, 5 Hz images (512×384) are used. In the localization phase, 1 Hz images (512×384) are used; For multi-frame localization, except for the current frame, almost stationary frames are skipped.

A. Mapping Performance

We first focus on the effectiveness of the mapping phase.

For large-scale mapping, obtaining precise global poses is fundamental. Nevertheless, this is a challenging task considering the intermittent degradation of GNSS observations in the experimental scenario. In Fig. 9, we show the pose estimation results of different approaches, including: 1) GNSS

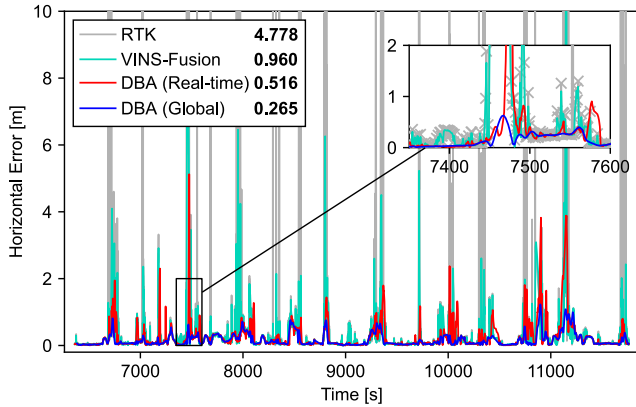


Fig. 9. Pose estimation results of the mapping phase. Monocular schemes are used for vision-based methods. The bold numbers are root mean square errors (RMSE) of the horizontal position error.

TABLE I
MAP STORAGE OF DIFFERENT MAPPING SCHEMES. IN CALCULATING THE DISTANCE, NON-REPEATING ONE-WAY ROADS ARE CONSIDERED.

Map Scheme	Storage (MB)	Storage per Km (MB)	Frame Number	Average Distance (m)
ORBSLAM3	6590.51 ¹	403.53	18768	0.870
HLoc (SP)	32206.7 ²	1971.99	27026	0.607
SF-Loc (0.4)	48.840 ³	2.990	1743	9.37
SF-Loc (0.3)	33.438 ⁴	2.047	1189	13.74

¹ 1439 MB (Local Desc.) + 719.6 MB (Global Desc.) + 4431 MB (Model)

² 27261 MB (Local Desc.) + 106.7 MB (Global Desc.) + 4839 MB (Model)

³ 37.67 MB (JPEG, 60) + 3.41 MB (Global Desc.) + 7.76 MB (Depth)

⁴ 25.81 MB (JPEG, 60) + 2.32 MB (Global Desc.) + 5.30 MB (Depth)

RTK, 2) VINS-Fusion (monocular VIO + RTK, final optimized trajectory) and 3) the proposed multi-sensor DBA scheme in real-time mode and global mode respectively. As can be found, the GNSS RTK results are noisy. Although decimeter-level accuracy is intermittently met, gross errors occur frequently. By integrating RTK with VIO, the VINS-Fusion scheme suppresses the gross errors to some extent. For the proposed DBA (real-time) scheme, by integrating visual DBA, inertial information and RTK in a tightly-coupled way, the GNSS errors are better mitigated. Furthermore, with the global optimization presented in Sect. IV-A, the position estimation error the DBA (global) scheme is mostly kept to below 1 m throughout the sequence, which ensures the decimeter-level lower bound of user-side absolute localization.

On the other hand, the generation of map data is looked into. As baselines, we test ORBSLAM3 and HLoc for the mapping task, which are both commonly used pipelines for visual mapping and re-localization. For ORBSLAM3, we simply use the monocular visual-inertial mode to process the sequence and save the map data in the Atlas format. The map storage is over 6 GB for the whole sequence, which is relatively heavy for practical applications. As for HLoc, we found it hard to achieve such large-scale SfM through the default COLMAP [54] + SIFT [55] pipeline. Instead, we directly use the ground-truth camera poses and perform feature extraction, matching and triangulation based on Superpoint and SuperGlue. The

TABLE II
RECALL AND ACCURACY OF THE COARSE RE-LOCALIZATION. MAP FRAMES WITH DIFFERENT SPARSITIES ($\Xi = 0.4$ AND $\Xi = 0.3$) ARE CONSIDERED RESPECTIVELY.

Ξ	Method	Recall @5 m	Recall @10 m	Recall @20 m	RMSE ¹ (m)
0.4	ORB + DBoW2	1.83%	3.11%	4.39%	38.79
	NetVLAD	43.09%	59.36%	65.35%	15.51
	AnyLoc	56.98%	79.09%	89.52%	13.91
	MixVPR	65.91%	89.67%	96.39%	7.67
	CosPlace18	64.35%	89.17%	94.67%	7.87
	CosPlace50	69.57%	93.34%	97.45%	7.12
	EigenPlaces18	69.07%	91.45%	96.17%	7.04
	EigenPlaces50	70.74%	92.73%	96.95%	6.52
	EigenPlaces18 (5)	69.35%	91.95%	96.67%	7.00
	EigenPlaces50 (5)	70.91%	93.28%	97.56%	6.54
	EigenPlaces18 (10)	69.52%	92.23%	96.95%	6.93
	EigenPlaces50 (10)	71.90%	94.50%	98.83%	5.96
0.3	EigenPlaces18 (SSS5)	72.68%	96.72%	99.83%	5.18
	EigenPlaces50 (SSS5)	75.62%	97.06%	99.89%	4.58
	EigenPlaces18 (SSS10)	73.96%	97.67%	100.00%	4.55
	EigenPlaces50 (SSS10)	73.57%	97.89%	100.00%	4.52
	ORB + DBoW2	1.17%	2.28%	3.11%	45.11
	NetVLAD	34.37%	53.41%	61.41%	16.40
	AnyLoc	48.45%	75.99%	87.78%	13.92
	MixVPR	53.91%	85.34%	94.84%	9.07
	CosPlace18	52.47%	82.51%	92.67%	8.74
	CosPlace50	56.08%	89.28%	96.50%	8.32
	EigenPlaces18	54.36%	85.12%	93.73%	8.05
	EigenPlaces50	56.75%	89.84%	97.06%	7.50
0.3	EigenPlaces18 (5)	54.75%	85.79%	94.50%	7.95
	EigenPlaces50 (5)	57.13%	90.28%	97.61%	8.75
	EigenPlaces18 (10)	54.91%	86.12%	94.95%	7.79
	EigenPlaces50 (10)	57.25%	90.56%	97.95%	7.00
	EigenPlaces18 (SSS5)	59.19%	92.84%	99.44%	5.73
	EigenPlaces50 (SSS5)	59.74%	93.56%	99.83%	5.63
	EigenPlaces18 (SSS10)	57.97%	92.84%	99.22%	5.50
	EigenPlaces50 (SSS10)	58.80%	93.78%	100.00%	5.48

¹ For RMSE calculation, only < 100 m cases are taken into account.

map storage is over 30 GB, which is 5 times larger than the ORBSLAM3 map. Such heavy map makes it hard to be applied to large-scale scenarios.

For the proposed SF-Loc, after global optimization, the visual structure frames are sparsified through co-visibility checking and inserted into the global map. Under such mechanism, the map is only updated when new viewpoints are available, and the number of the map frames wouldn't grow if the vehicle revisited the region several times. As mentioned in Sect. IV-B, the co-visibility threshold Ξ directly controls the map sparsity. We test different co-visibility thresholds (0.3 or 0.4) for map construction. Finally, the data size of the map is around 3 MB per kilometer for $\Xi = 0.4$ and around 2 MB per kilometer for $\Xi = 0.3$, which is 1~3 orders of magnitude smaller than that of the aforementioned methods. Later, we will discuss how high-precision localization can be achieved under such sparsified and compressed map information.

B. Localization Performance

As to user-side localization, we check the coarse-to-fine localization performance of the proposed system.

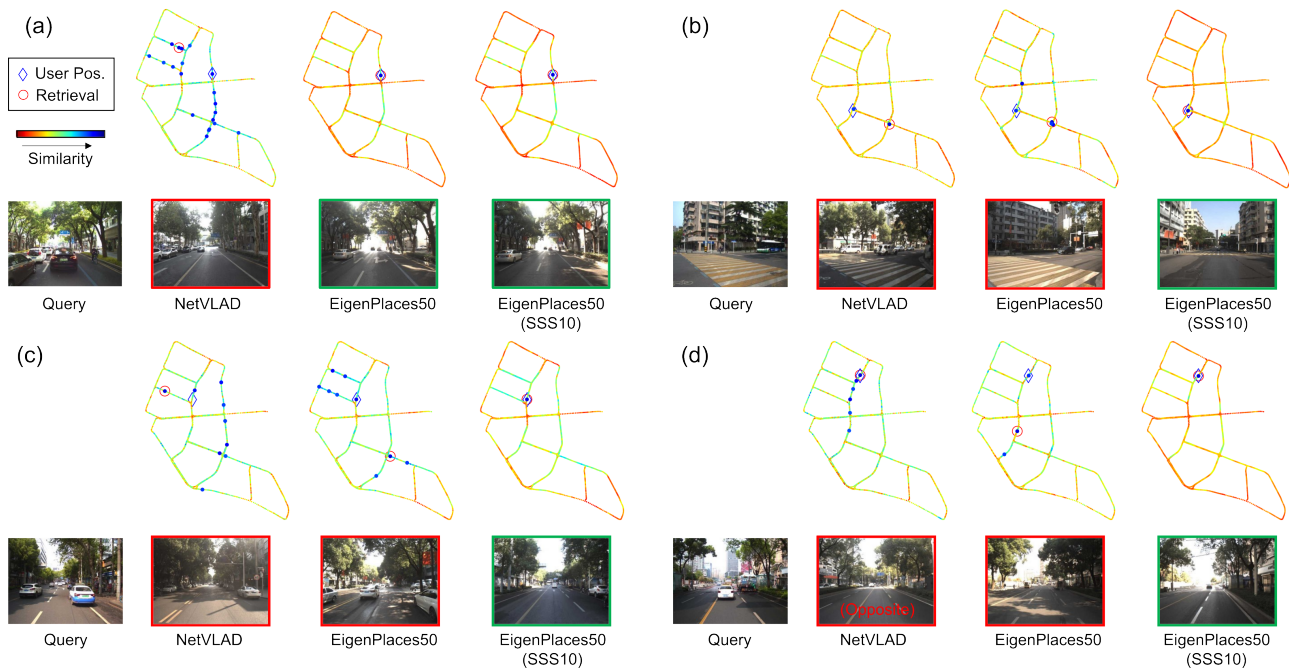


Fig. 10. Example cases of the coarse localization. The green borderline indicates correct retrieval, while the red borderline indicates wrong retrieval (large position error or heading error). High-similarity candidates (local minima and $\sigma < \sigma_{\min} + 0.15(\sigma_{\max} - \sigma_{\min})$) are marked using larger circles.

1) *Coarse Localization*: The coarse localization is based on the map frames generated by SF-Loc. We show the recall rates of different schemes in TABLE II, including the classic ORB + DBoW2 implementation [8] and commonly used DNN-based methods (NetVLAD [33], AnyLoc [37], MixVPR [52], CosPlace [35], EigenPlaces [36]). For CosPlace and EigenPlaces, different backbones (ResNet18 or ResNet50 [56]) are considered. Based on the state-of-the-art lightweight model EigenPlaces, we employ the proposed SSS technique to aggregate spatial-temporal information, termed as “EigenPlaces (SSSK)”. To verify the effectiveness of the proposed SSS metric, we also implement a naive multi-frame VPR model by clustering the top- K candidates of multiple queries and choosing the candidate belonging to the largest cluster as the result, termed as “EigenPlaces (K)”.

Taking the $\Xi = 0.4$ case as example, several typical query cases are shown in Fig. 10, which indicate the challenge of re-localization, with dynamic objects, light condition variation and high-ambiguity environmental patterns. In such scenarios, the traditional handcrafted place recognition method (ORB + DBoW2) becomes almost useless, as the low-level appearance of the environment changes significantly for the cross-season sequences. For learning-based methods, the classic NetVLAD achieves 59% 10 m recall, while more modern methods (e.g., CosPlace, EigenPlaces and MixVPR) can generally achieve 90% 10 m recall. Although 90% recall seems good enough for place recognition, it can’t serve as a reliable information source for the localization task, especially for unmanned systems. By naively combining the VPR results of multiple frames, the 10/20 m recall can increase by around 1%. In contrast, with the proposed SSS-based multi-frame VPR technique, the 10/20 m recall can increase by 5%. Especially, for the SSS10 scheme, the 20 m recall can achieve 100%, both

for ResNet50 and ResNet18 backbones. Compared to single-frame VPR methods, the introduction of SSS greatly improves the reliability of the coarse localization information, which is crucial for further fine localization.

We also list the results based on a more sparse map with co-visibility threshold $\Xi = 0.3$. Generally, the recall is noticeably lower than the $\Xi = 0.4$ case, while the EigenPlaces50 (SSS10) scheme can still achieve 93.78%/100% 10m/20m recall.

2) *Fine Localization*: As to the evaluation of fine localization, we test the re-localization modes of ORB-SLAM3 and HLoc as the baselines, and also test GNSS-based schemes for reference, including single point positioning (SPP) and VINS-Fusion (stereo VIO + SPP). For the proposed SF-Loc, we test both single-frame and multi-frame re-localization modes. For multi-frame re-localization, the user-side relative poses are provided by stereo VIO. The factor graph optimization implementation in Sect. V-B is used. For comparison, we also test PnP with RANSAC upon the SF-Loc map.

For ORB-SLAM3 and HLoc, the coarse-to-fine localization is performed based on their own pipeline and map data (corresponding to TABLE I). For SF-Loc, the map data generated with different co-visibility thresholds ($\Xi = 0.3/0.4$) are considered, and the coarse localization results of EigenPlaces50 (SSS10) are used.

As can be seen from Fig. 11, ORB-SLAM3 can hardly perform successful re-localization, as both the coarse and fine localization phases are challenged by the significant appearance variation. For HLoc and SF-Loc, decimeter-level localization is achievable when the map matching is well performed, while outliers with several-meter error are also present, which generally correspond to the ambiguous scenarios. It is noted that HLoc performs better than single-frame SF-loc, which is reasonable as the HLoc map contains many more frames

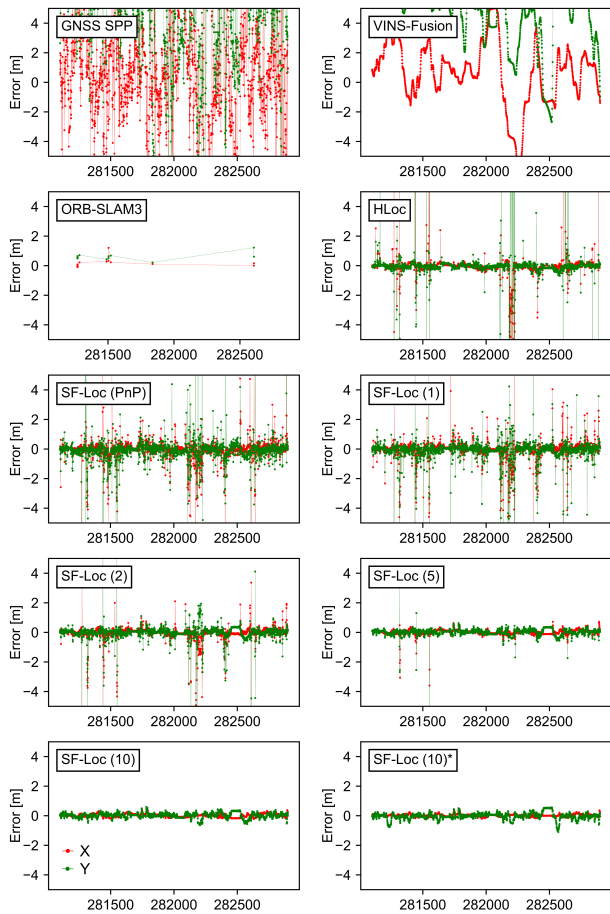


Fig. 11. Horizontal position errors of the fine localization. For SF-Loc, the $\Xi = 0.4$ map is used. See TABLE III for detailed description.

(see TABLE I) and stores the fine descriptors extracted from the lossless raw images. In contrast, SF-Loc only uses highly compressed images at the user end. In addition, we witness an improvement of using factor graph optimization than using classic PnP method for the one-frame pose estimation, as the noise model can be better specialized considering the low-resolution depth and the noise of feature matching.

It is impressive that, the localization accuracy of SF-Loc can be greatly improved by integrating multi-frame information. The examples that multi-frame observations lead to better data association and localization results are depicted in Fig. 12. As can be seen, the introduction of multi-frame information not only help bridge the low-correspondence cases, but also help adjust the inlier set of correspondences and improve the geometric configuration, leading to more robust pose estimation. For the $\Xi = 0.4$ map, with 10-frame FGO, the SF-Loc achieves 99.0% availability@0.5 m and a RMSE of 0.209 m. As to the absolute positioning accuracy considering the error of map frames, the availability@0.5 m is 91.62% and the RMSE is 0.247 m, which mainly satisfy the demand of decimeter-level localization accuracy. When the map becomes sparser ($\Xi = 0.3$), the multi-frame localization performance remains almost unchanged, which shows the possibility of harder map compression in the cost of some redundancy.

Finally, we show the time consumption statistics of user-

TABLE III
ACCURACY OF THE FINE RE-LOCALIZATION. HORIZONTAL POSITION ERRORS ARE EVALUATED.

Map	Method ¹	Avail. @0.5 m	Avail. @1.0 m	Avail. @5.0 m	RMSE ² (m)
-	SPP	0.11%	0.44%	19.16%	8.059
-	VINS-Fusion	0.00%	0.00%	28.98%	6.506
PC (ORB)	ORB-SLAM3	0.33%	1.28%	1.55%	0.997
PC (SP)	HLoc	88.95%	93.00%	96.39%	0.503
SF (0.4)	PnP	70.41%	85.95%	98.17%	0.852
	FGO (1)	78.46%	88.78%	98.28%	0.825
	FGO (2)	87.23%	94.00%	99.17%	0.604
	FGO (5)	96.39%	99.33%	99.89%	0.298
	FGO (10)	99.00%	100.00%	100.00%	0.209
SF (0.3)	FGO (10)*	91.62%	99.67%	100.00%	0.247
	PnP	68.41%	85.01%	96.45%	0.881
	FGO (1)	74.68%	86.79%	96.84%	0.807
	FGO (2)	86.12%	93.50%	99.22%	0.577
	FGO (5)	94.45%	99.22%	100.00%	0.323
SF (0.3)	FGO (10)	97.89%	100.00%	100.00%	0.213
	FGO (10)*	94.73%	99.67%	100.00%	0.248

¹ For ORB-SLAM3, HLoc and SF-Loc without the "*" notation, relative pose estimation between the query frame and the map frame is evaluated. The "*" notation means that the absolute position error is evaluated, i.e., the pose error of the map frame (see Fig. 9) is taken into account.
² For RMSE calculation, only < 5 m cases are taken into account.

TABLE IV
TIME COST OF DIFFERENT MODULES IN USER-SIDE LOCALIZATION.

Phase	Module	Time cost (ms)
Coarse Localization ¹	VPR Descriptor	5.7
	Retrieval	27.3
Fine Localization ²	Local Feature Extraction	33.0
	Feature Matching	30.3
	Pose Estimation	32.2

¹ Using "EigenPlaces50 (SSS10)" scheme in TABLE II.
² Using "SF-Loc (10)" scheme in TABLE III.

side localization in TABLE IV, which is tested on a laptop with Nvidia RTX 4080 GPU.

VII. CONCLUSION

In this paper, we propose a vision-centered mapping and localization framework based on the map representation of visual structure frames. The highlight of the system is the lightweight map storage by making the frame data compact and keeping the sparsity, while can still support high-recall, high-accuracy localization through the utilization of user-side multi-frame information.

In later work, we will investigate the application of the system to indoor environments, and improve the system performance by introducing the power of visual foundation models.

ACKNOWLEDGMENTS

The implemented SF-Loc is developed by the GREAT Group, School of Geodesy and Geomatics, Wuhan University. The numerical calculations in this paper have been done on the supercomputing system at the Supercomputing Center of Wuhan University.

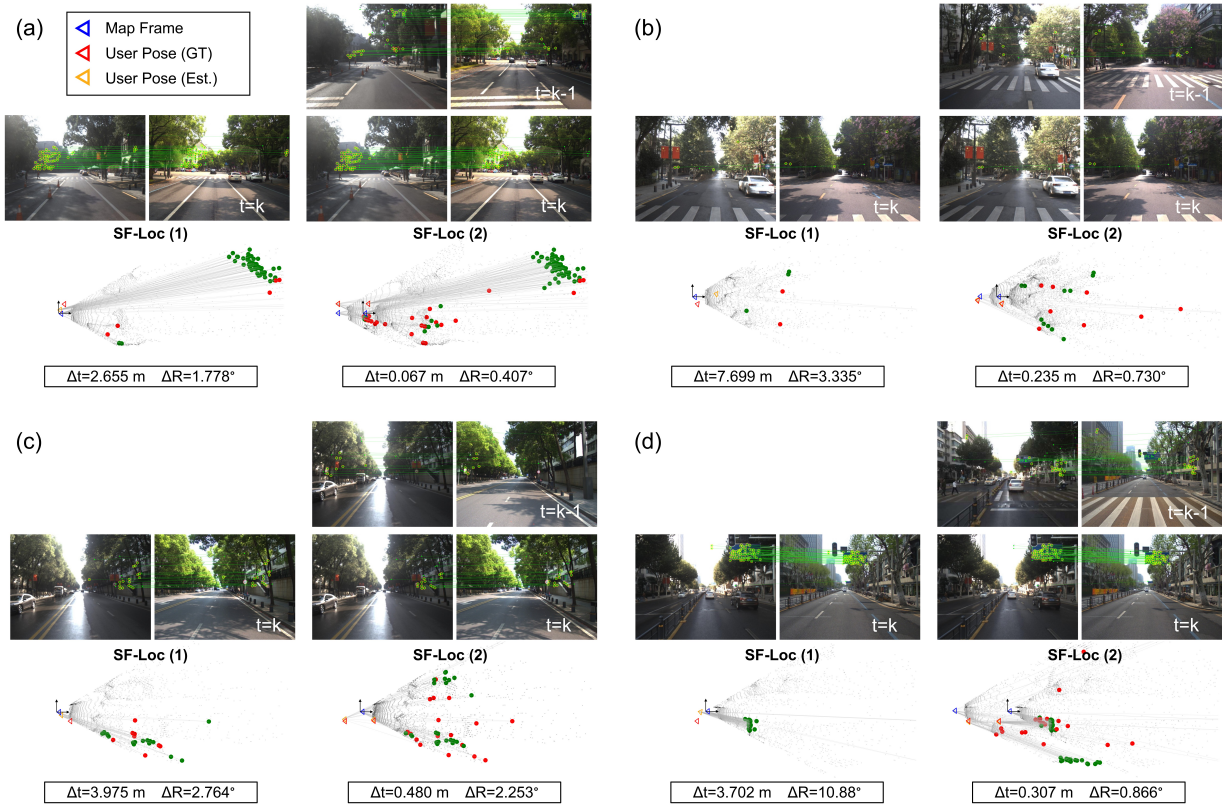


Fig. 12. Examples that demonstrate how multi-frame information contributes to the fine localization. In every panel, the left column corresponds to the **SF-Loc (1)** scheme, while the right column corresponds to the **SF-Loc (2)** scheme. In the bird’s eye view plots, the green markers indicate inliers while the red ones indicate outliers.

REFERENCES

- [1] C. Cadena et al., “Past, Present, and Future of Simultaneous Localization and Mapping: Toward the Robust-Perception Age,” *IEEE Trans. Robot.*, vol. 32, no. 6, pp. 1309-1332, Dec. 2016.
- [2] I. Ullah, D. Adhikari, H. Khan, M. S. Anwar, S. Ahmad, and X. Bai, “Mobile robot localization: Current challenges and future prospective,” *Comput. Sci. Rev.*, vol. 53, p. 100651, 2024.
- [3] X. Li et al., “Continuous and precise positioning in urban environments by tightly coupled integration of GNSS, INS and vision,” *IEEE Robot. Autom. Lett.*, vol. 7, no. 4, pp. 11458–11465, 2022.
- [4] W. Wen and L.-T. Hsu, “Towards robust GNSS positioning and real-time kinematic using factor graph optimization,” in *ICRA 2021*, pp. 5884–5890.
- [5] A. Chalvatzaras, I. Pratikakis, and A. A. Amanatiadis, “A survey on map-based localization techniques for autonomous vehicles,” *IEEE Trans. Intell. Veh.*, vol. 8, no. 2, pp. 1574–1596, 2022.
- [6] P. Yin et al., “General Place Recognition Survey: Towards Real-World Autonomy,” May 08, 2024, arXiv: arXiv:2405.04812.
- [7] Z. Zhang, M. Xu, W. Zhou, T. Peng, L. Li, and S. Poslad, “BEV-Locator: An End-to-end Visual Semantic Localization Network Using Multi-View Images,” Nov. 27, 2022, arXiv: arXiv:2211.14927.
- [8] C. Campos, R. Elvira, J. J. G. Rodríguez, J. M. M. Montiel and J. D. Tardós, “ORB-SLAM3: An Accurate Open-Source Library for Visual, Visual-Inertial, and Multimap SLAM,” *IEEE Trans. Robot.*, vol. 37, no. 6, pp. 1874-1890, Dec. 2021.
- [9] Sarlin, Paul-Edouard, Cesar Cadena, Roland Siegwart, and Marcin Dymczyk, “From coarse to fine: Robust hierarchical localization at large scale,” in *CVPR 2019*, pp. 12716-12725.
- [10] L. Xu, C. Feng, V. R. Kamat, and C. C. Menassa, “An Occupancy Grid Mapping enhanced visual SLAM for real-time locating applications in indoor GPS-denied environments,” *Autom. Constr.*, vol. 104, pp. 230–245, Aug. 2019.
- [11] P.-E. Sarlin, E. Trulls, M. Pollefeys, J. Hosang, and S. Lynen, “Snap: Self-supervised neural maps for visual positioning and semantic understanding,” in *NeurIPS 2024*.
- [12] H. Zhai et al., “SplatLoc: 3D Gaussian Splatting-based Visual Localization for Augmented Reality,” Sep. 21, 2024, arXiv: arXiv:2409.14067.
- [13] A. J. Davison, I. D. Reid, N. D. Molton, and O. Stasse, “MonoSLAM: Real-time single camera SLAM,” *IEEE Trans. Pattern Anal. Mach. Intell.*, vol. 29, no. 6, pp. 1052–1067, 2007.
- [14] A. Pumarola, A. Vakhtov, A. Agudo, A. Sanfeliu, and F. Moreno-Noguer, “PL-SLAM: Real-time monocular visual SLAM with points and lines,” in *ICRA 2017*, pp. 4503–4508.
- [15] J. Engel, V. Koltun, and D. Cremers, “Direct sparse odometry,” *IEEE Trans. Pattern Anal. Mach. Intell.*, vol. 40, no. 3, pp. 611–625, 2017.
- [16] T. Qin, P. Li, and S. Shen, “Vins-mono: A robust and versatile monocular visual-inertial state estimator,” *IEEE Trans. Robot.*, vol. 34, no. 4, pp. 1004-1020, 2018.
- [17] S. Leutenegger, S. Lynen, M. Bosse, R. Siegwart, P. Furgale, “Keyframe-based visual-inertial odometry using nonlinear optimization,” *Int. J. Robot. Res.*, vol. 34, no. 3, pp. 314-334, 2014.
- [18] A. I. Mourikis and S. I. Roumeliotis, “A Multi-State Constraint Kalman Filter for Vision-aided Inertial Navigation,” in *ICRA 2007*, pp. 3565-3572.
- [19] S. Cao, X. Lu, and S. Shen, “GVINS: Tightly coupled GNSS–visual–inertial fusion for smooth and consistent state estimation,” *IEEE Trans. Robot.*, vol. 38, no. 4, pp. 2004–2021, 2022.
- [20] K. Wu, C. Guo, G. Georgiou, and S. I. Roumeliotis, “Vins on wheels,” in *ICRA 2017*, pp. 5155-5162.
- [21] A. Cramariuc et al., “maplab 2.0—a modular and multi-modal mapping framework,” *IEEE Robot. Autom. Lett.*, vol. 8, no. 2, pp. 520–527, 2022.
- [22] Y. Tian, Y. Chang, F. H. Arias, C. Nieto-Granda, J. P. How, and L. Carlone, “Kimera-multi: Robust, distributed, dense metric-semantic slam for multi-robot systems,” *IEEE Trans. Robot.*, vol. 38, no. 4, 2022.
- [23] Z. Zhu et al., “Nicer-slam: Neural implicit scene encoding for rgb slam,” Feb. 2023, arXiv:2302.03594.
- [24] H. Matsuki, R. Murai, P. H. Kelly, and A. J. Davison, “Gaussian splatting slam,” in *CVPR 2024*, pp. 18039–18048.
- [25] Z. Teed, L. Lipson, and J. Deng, “Deep patch visual odometry,” in *NeurIPS 2024*.

- [26] Z. Teed and J. Deng, “Droid-slam: Deep visual slam for monocular, stereo, and rgb-d cameras,” in *NeurIPS 2021*, pp. 16558–16569.
- [27] S. Li, S. Liu, Q. Zhao and Q. Xia, “Quantized Self-Supervised Local Feature for Real-Time Robot Indirect VSLAM,” in *IEEE/ASME Transactions on Mechatronics*, vol. 27, no. 3, pp. 1414–1424, June 2022.
- [28] S. Wang, R. Clark, H. Wen, and N. Trigoni, “Deepvo: Towards end-to-end visual odometry with deep recurrent convolutional neural networks,” in *ICRA 2017*, pp. 2043–2050.
- [29] J. Jiao, J. Jiao, Y. Mo, W. Liu and Z. Deng, “MagicVO: An End-to-End Hybrid CNN and Bi-LSTM Method for Monocular Visual Odometry,” *IEEE Access*, vol. 7, pp. 94118–94127, 2019.
- [30] D. Gálvez-López, J. D. Tardos. Bags of binary words for fast place recognition in image sequences. *IEEE Trans. Robot.*, vol. 28, no.5, pp. 1188–1197, 2012.
- [31] H. Jégou, M. Douze, C. Schmid, and P. Pérez, “Aggregating local descriptors into a compact image representation,” in *CVPR 2010*, pp. 3304–3311.
- [32] M. J. Milford and G. F. Wyeth, “SeqSLAM: Visual route-based navigation for sunny summer days and stormy winter nights,” in *ICRA 2012*, pp. 1643–1649.
- [33] R. Arandjelović, P. Gronat, A. Torii, T. Pajdla and J. Sivic, “NetVLAD: CNN Architecture for Weakly Supervised Place Recognition,” *IEEE Trans. Pattern Anal. Mach. Intell.*, vol. 40, no. 6, pp. 1437–1451, June 2018.
- [34] R. Wang, Y. Shen, W. Zuo, S. Zhou, and N. Zheng, “Transvpr: Transformer-based place recognition with multi-level attention aggregation,” in *CVPR 2022*, pp. 13648–13657.
- [35] G. Berton, C. Masone, and B. Caputo, “Rethinking visual geolocalization for large-scale applications,” in *CVPR 2022*, pp. 4878–4888.
- [36] G. Berton, G. Trivigno, B. Caputo, and C. Masone, “Eigenplaces: Training viewpoint robust models for visual place recognition,” in *ICCV 2023*, pp. 11080–11090.
- [37] N. Keetha et al., “AnyLoc: Towards Universal Visual Place Recognition,” *IEEE Robot. Autom. Lett.*, vol. 9, no. 2, pp. 1286–1293, Feb. 2024.
- [38] T. Qin, S. Cao, J. Pan, and S. Shen, “A general optimization-based framework for global pose estimation with multiple sensors,” arXiv:1901.03642, 2019.
- [39] E. Arnold et al., “Map-Free Visual Relocalization: Metric Pose Relative to a Single Image,” in *ECCV 2022*.
- [40] S. Yang and S. Scherer, “Cubeslam: Monocular 3-d object slam,” *IEEE Trans. Robot.*, vol. 35, no. 4, pp. 925–938, 2019.
- [41] A. Adkins, T. Chen, and J. Biswas, “ObVi-SLAM: Long-Term Object-Visual SLAM,” *IEEE Robot. Autom. Lett.*, vol. 9, no. 3, pp. 2909–2916, Mar. 2024.
- [42] Y. Wang, C. Jiang and X. Chen, “GOReloc: Graph-Based Object-Level Relocalization for Visual SLAM,” *IEEE Robot. Autom. Lett.*, vol. 9, no. 10, pp. 8234–8241, Oct. 2024.
- [43] Y. Yu, P. Yun, B. Xue, J. Jiao, R. Fan and M. Liu, “Accurate and Robust Visual Localization System in Large-Scale Appearance-Changing Environments,” in *IEEE/ASME Transactions on Mechatronics*, vol. 27, no. 6, pp. 5222–5232, Dec. 2022.
- [44] P.-E. Sarlin et al., “Orienternet: Visual localization in 2d public maps with neural matching,” in *CVPR 2023*, pp. 21632–21642.
- [45] O. Kwon et al., “WayLL: Image-based Indoor Localization with Wayfinding Maps,” in *ICRA 2024*, pp. 6274–6281.
- [46] Wallace, Gregory K. “The JPEG still picture compression standard.” *Communications of the ACM*, vol. 34, no. 4, pp. 30–44, 1991.
- [47] F. Dellaert and M. Kaess, *Factor Graphs for Robot Perception*. Foundations, 2017.
- [48] Y. Zhou, X. Li, S. Li, X. Wang, S. Feng, and Y. Tan, “DBA-Fusion: Tightly Integrating Deep Dense Visual Bundle Adjustment With Multiple Sensors for Large-Scale Localization and Mapping,” *IEEE Robot. Autom. Lett.*, vol. 9, no. 7, pp. 6138–6145, Jul. 2024.
- [49] C. Forster, L. Carlone, F. Dellaert and D. Scaramuzza, “On-manifold preintegration for real-time visual-inertial odometry,” *IEEE Trans. Robot.*, vol. 33, no. 1, pp. 1–21, Feb. 2017.
- [50] P. Lindenberger, P.-E. Sarlin, and M. Pollefeys, “Lightglue: Local feature matching at light speed,” in *ICCV 2023*, pp. 17627–17638.
- [51] P.-E. Sarlin, D. DeTone, T. Malisiewicz, and A. Rabinovich, “Superglue: Learning feature matching with graph neural networks,” in *CVPR 2020*, pp. 4938–4947.
- [52] A. Ali-Bey, B. Chaib-Draa, and P. Giguere, “Mixvpr: Feature mixing for visual place recognition,” in *WACV 2023*, pp. 2998–3007.
- [53] D. DeTone, T. Malisiewicz, and A. Rabinovich, “Superpoint: Self-supervised interest point detection and description,” in *CVPRW 2018*, pp. 224–236.
- [54] J. L. Schonberger and J.-M. Frahm, “Structure-from-motion revisited,” in *CVPR 2016*, pp. 4104–4113.
- [55] D. G. Lowe, “Distinctive Image Features from Scale-Invariant Key-points,” *Int. J. Comp. Vis.*, vol. 60, no. 2, pp. 91–110, Nov. 2004.
- [56] K. He, X. Zhang, S. Ren, and J. Sun, “Deep residual learning for image recognition,” in *CVPR 2016*, pp. 770–778.



Yuxuan Zhou (Graduate Student Member, IEEE) received the M.Eng. degree in navigation engineering from Wuhan University, Wuhan, China, in 2022, where he is currently pursuing the Ph.D. degree with the School of Geomatics and Geodesy. His current research interests include integrated navigation systems and multi-sensor fusion



Xingxing Li received the B.S. degree from the School of Geodesy and Geomatics, Wuhan University, and the Ph.D. degree from the Department of Geodesy and Remote Sensing, German Research Centre for Geosciences (GFZ). He is currently a Professor with Wuhan University. His current research interests include GNSS precise data processing and multi-sensor navigation.



Shengyu Li (Graduate Student Member, IEEE) received the M.Eng. degree in navigation engineering from Wuhan University, Wuhan, China, in 2022, where he is currently pursuing the Ph.D. degree with the School of Geomatics and Geodesy. His current research interests include integrated navigation systems and multi-sensor fusion.



Chunxi Xia received the M.Eng. degree in navigation engineering from Wuhan University, Wuhan, China, in 2023, where he is currently pursuing the Ph.D. degree with the School of Geomatics and Geodesy. His current research interests include vision-based navigation and multi-sensor fusion.



Xuanbin Wang received the M.Eng. degree in navigation engineering from Wuhan University, Wuhan, China, in 2021. He is currently pursuing the Ph.D. degree with the School of Geomatics and Geodesy, Wuhan University. His current research focuses on integrated navigation system and multi-sensor fusion.



Shaoquan Feng received the M.Eng. degree in geodesy and survey engineering from Wuhan University, Wuhan, China, in 2020, where he is currently pursuing the Ph.D. degree with the School of Geomatics and Geodesy. His current research interests include multi-object tracking, integrated navigation systems, and multi sensor fusion